Estimation of Sea Surface Temperature From Landsat-8 Measurements via Neural Networks

Jinyan Xie, Zhongping Lee, *Member, IEEE*, Xu Li, Daosheng Wang, Caiyun Zhang, Yufang Wu, Xiaolong Yu, and Zhihuang Zheng

***Abstract*—The Landsat-8 Collection 2 provides Level-2 surface temperature product (L8-L2ST) at a spatial resolution of 30 m, catering to various applications. However, discrepancies in the spatial resolution of certain parameters involved in L8-L2ST production often result in noticeable "checkerboard" patterns in images over oceanic waters. To enhance the accuracy of sea surface temperature (SST) products derived from the Landsat-8 measurements, this study introduces a neural network (NN) based algorithm for the estimation of SST. By sidestepping the conventional radiative-transfer-based method, which relies on numerous auxiliary data products, the SST generated by the NN-based algorithm could avoid the "checkerboard" issues encountered in the L8-L2ST products. Compared to the reference MODIS SST products, the root mean square error (RMSE) of NN-based SST is 0.7 °C, whereas the RMSE of L8-L2ST is 1.42 °C. In comparison to buoy data, the RMSE of this method is 1.18 °C, while the RMSE of L8-L2ST is 2 °C. This work thus presents a valuable framework for acquiring more consistent and better-quality SST products from Landsat-8 measurements.**

***Index Terms*—Landsat-8, neural network (NN), sea surface temperature (SST), thermal infrared, top-of-atmosphere radiance.**

I. Introduction

SURFACE temperature (ST) of the Earth system plays a vital role in ecosystems [1] and climate change research [2]. It is a key element in studying atmospheric circulation [3], climate models [4], and phenomena such as El Niño [5]. For the ocean environment, sea surface temperature (SST) is not only a key parameter driving ocean dynamics, but it also directly affects the distribution, growth, and functionality of marine organisms [6]. Monitoring and understanding SST variations are crucial for the effective management of marine resources, ecological conservation, and tackling potential challenges due to climate change. Thus, the international community has spent great effort to obtain SST measurements of the global oceans via floats, buoys, Argos, and satellite missions.

Since 1978, Advanced Very High Resolution Radiometer (AVHRR) has been a reliable source of high-quality SST products, succeeded by Moderate Resolution Imaging Spectroradiometer (MODIS) and Visible Infrared Imaging Radiometer Suite (VIIRS) from the US, Sentinel-3 from Europe, and HY-1C/1D from China, among others. However, these satellite systems typically operate at kilometer-scale spatial resolutions. Coastal and nearshore water environments, characterized by intricate topography, feature high demands on high-spatial-resolution SST products for fisheries, environmental monitoring, as well as modeling of circulation dynamics. Landsat-8, launched in 2013, addresses this need with two thermal infrared channels with a spatial resolution of 100 m (products are resampled to 30 m), and provides excellent SST products with stable data sources, making Landsat-8 a valuable and practical tool for monitoring SST in coastal and nearshore waters [7], [8], [9].

A satellite sensor measures top-of-atmosphere radiance (L_t), where L_t in the infrared is converted to SST through algorithms. At present, SST retrieval algorithms mainly include single-channel and multichannel algorithms [10]. Single-channel algorithms, which are also employed to process Landsat-8 data, face a challenge in obtaining high-quality SST, as it is necessary to have concurrent and accurate measurements of water vapor content in the atmosphere [11]. Multichannel algorithms [12] utilize differences in atmospheric effects across various thermal infrared channels to mitigate atmospheric interference and derive better SST products than the single-channel scheme [13]. Further, split-window algorithms [14] reduce the dependence on atmospheric parameters, requiring fewer input variables, exhibiting high computational efficiency, and achieving more accurate retrievals. This algorithm, however, demands a substantial amount of ground-truth SST data to calibrate the algorithm coefficients. Despite its successful application in MODIS, it has been shown that for Landsat-8, this method has a large error and still needs further improvement [15]. In recent years, with the development of Big Data technology, numerous methods based on statistical regression [16], machine learning [17], [18], and data fusion [19] have emerged to estimate SST.

Given the advanced capability of Landsat-8, many researchers have attempted to obtain SST from Landsat-8 [15], [20], [21], [22], [23], and single-channel algorithms have been employed

Received 8 March 2024; revised 30 April 2024 and 27 June 2024; accepted 20 July 2024. Date of publication 3 September 2024; date of current version 20 September 2024. This work was supported in part by the Science and Technology Program of Fujian Province, China, under Grant 2023Y4001, in part by the Science and Technology Progam of Xiamen, China, under Grant 3502Z20226021, and in part by the National Natural Science Foundation of China under Grant 41941008, Grant 41890803, and Grant 41830102. *(Corresponding author: Zhongping Lee.)*

Jinyan Xie, Zhongping Lee, Xu Li, Daosheng Wang, Caiyun Zhang, and Xiaolong Yu are with the State Key Laboratory of Marine Environmental Science, College of Ocean and Earth Sciences, Xiamen University, Xiamen 361102, China (e-mail: jyxie@stu.xmu.edu.cn; zhongping.lee@umb.edu; xliyy@stu.xmu.edu.cn; dswang@xmu.edu.cn; cyzhang@xmu.edu.cn; xlyu@xmu.edu.cn).

Yufang Wu is with the Xiamen Environmental Monitoring Station, Xiamen 361022, China (e-mail: xiaoran19992018@163.com).

Zhihuang Zheng is with the Fujian Jingwei Digital Technology Company, Ltd., Fuzhou 350003, China (e-mail: 273011974@qq.com).

Digital Object Identifier 10.1109/JSTARS.2024.3453908

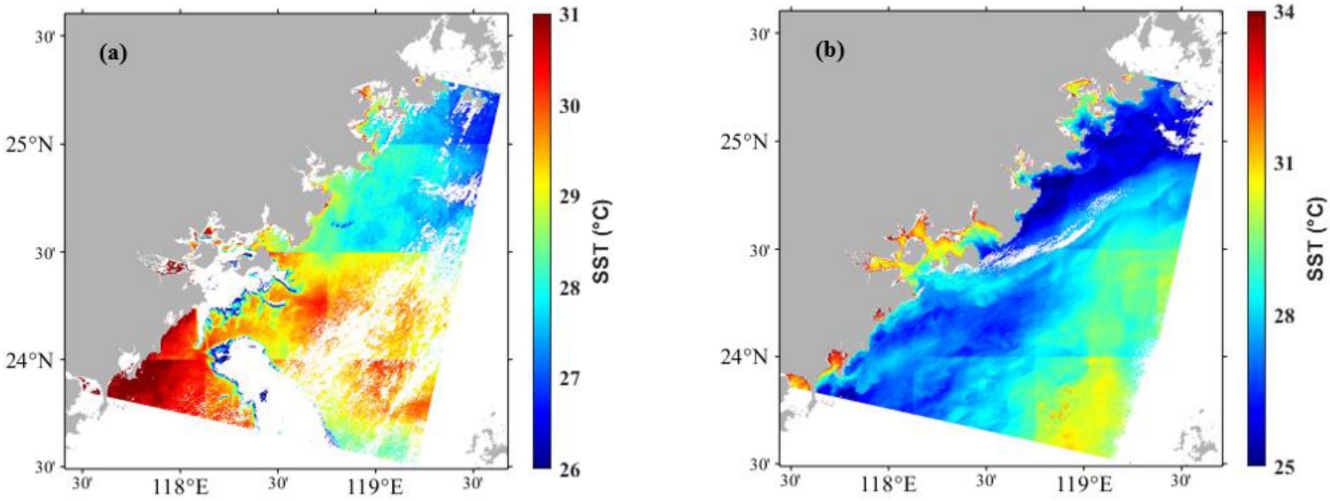

Fig. 1. Example of L8-L2ST products over Fujian coast, China, acquired on (a) 30 September 2022 and (b) 9 July 2021, that encountered the "checkerboard" patterns.

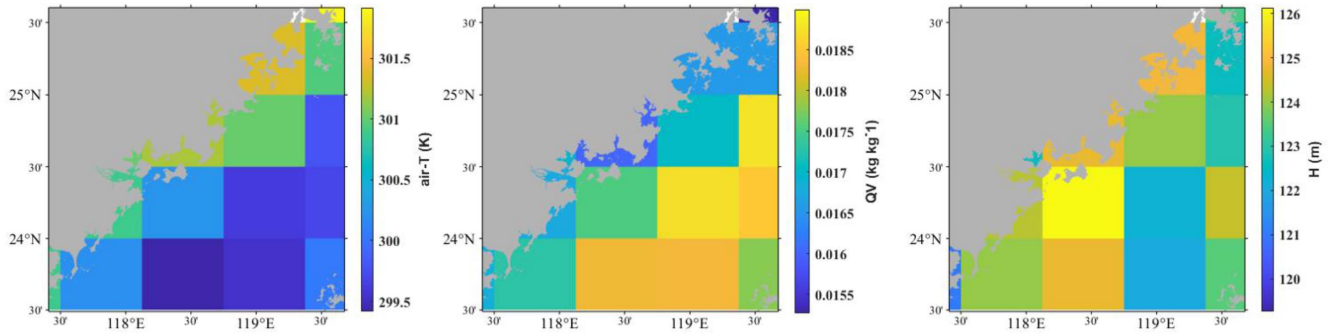

Fig. 2. FP-IT atmospheric reanalysis data (air-T, QV, and H) have the same "checkerboard" phenomenon due to its low spatial resolution, which is used to develop input used in moderate resolution atmospheric transmission software.

for this objective. However, while applying the Landsat-8 Collection 2 Level 2 ST (L8-L2ST hereafter) products released by the United States Geological Survey (USGS), quite often (∼40% of L8-L2ST images we utilized) it is found that there is a "checkerboard" pattern in the SST images, where Fig. 1 shows a few examples. This is not caused by Landsat-8 stray light, as it does not show this kind of pattern [24].

To trace back the source of this pattern, we analyzed the L_t data of Landsat-8 Band #10 that is used to produce L8-L2ST and did not find such a "checkerboard" issue, thus the patterns shown in Fig. 1 indicate that it arises from the processing steps. In particular, the generation of L8-L2ST product is based on radiative transfer and involves a wide range of auxiliary inputs, such as emissivity calculated from Global Emissivity Data (GED) obtained by the Advanced Spaceborne Thermal Emission and Reflection Radiometer (ASTER), and atmospheric information from Forward Processing for Instrument Teams (FP-IT) analysis. FP-IT products are atmospheric reanalysis data, which include several used by USGS to calculate L8-L2ST, such as air temperature (air-T), specific humidity (QV), and geopotential height (H). It is beyond the scope of this effort to pinpoint the exact sources related to the "checkerboard" patterns, but we speculate that the low-resolution (0.625° × 0.5°) inputs (such as air-T, QV, and H), which were resampled to Landsat-8 grid, might be the sources. In Fig. 2, we use the product of 30 September 2022 [corresponding to Fig. 1(a) for L8-L2ST] as an example to showcase the nonsmoothness of air temperature (air-T), specific humidity (QV), and geopotential height (H) data. The pixels, with a resolution of 0.625° × 0.5°, align well with the "checkerboard" patterns observed in the L8-L2ST products.

In this study, to produce improved SST data product from Landsat-8 measurements, we bypassed the traditional single-band or split-window scheme for the estimation of SST from Landsat-8 infrared L_t measurements, rather used neural network (NN) scheme, termed NN_for_L8-SST hereafter, to estimate SST. A wide range of studies have demonstrated the excellent power of NNs in remote sensing practices [25], [26], [27], where the key is to have adequate and inclusive data to train the desired NN. In addition, researchers have demonstrated that NNs-based algorithms for estimating SST offer higher accuracy compared to other methods [28]. At present, because of the existence of many high-quality SST products (e.g., MODIS, VIIRS), although at a relatively low spatial resolution, there is thus no shortage of

matchup data between Landsat-8 thermal measurements and other satellite SST products. We therefore, as an example, use MODIS SST as the reference and develop a neural-networks scheme to obtain high-resolution SST products from Landsat-8 measurements, where more consistent, and quality-improved SST products are achieved.

II. Data

A. Landsat-8 Data

Landsat-8 is equipped with the operational land imager (OLI) and the thermal infrared sensor (TIRS). TIRS has two bands, with one band (Band #10) having a wavelength range of 10.60–11.19 μm and another band (Band #11) with a wavelength range of 11.50–12.51 μm. The spatial resolution of TIRS is 100 m, but its product is resampled to 30 m to match that of OLI. Landsat-8 Collection 2 was released by USGS at the end of 2020, which included standard Level 2 surface reflectance and ST products [29]. They utilize a radiative transfer algorithm to obtain Level-2 ST products. Research has shown that significant differences arise due to the use of a lower emissivity value for water targets and differences in atmospheric parameter retrieval [29]. We obtained Landsat-8 Collection 2 Level 1 (C2L1) radiance (L_t) data via the United States Geological Survey's EarthExplorer platform.[1] Alongside L_t values, observation information such as solar zenith angle (SOZ), solar azimuth angle (SOA), satellite zenith angle (SAZ), and satellite azimuth angle (SAA) were also acquired. To mask out pixels influenced by cloud, we excluded pixels with cloud albedo (α_{cloud}) greater than 0.018 [30], where α_{cloud} was computed using SeaDAS 8.1.0.

B. MODIS Data

For demonstration purposes, while there are many satellite SST products available, the SST product from the MODIS-Aqua matching the location and time of Landsat-8 was used as a reference or standard. We obtained MODIS Level-2 SST products from NASA's OceanColor Web,[2] supported by the Ocean Biology Processing Group at NASA's Goddard Space Flight Center. The SST product has a temporal resolution of 1 day and a spatial resolution of 1 km. We excluded SST data of low quality with qual_sst values of 2 (questionable), 3 (bad), and 4 (not processed).

Assuming negligible SST changes over a short period, we utilized a time window of 3 h between Landsat-8 TIRS and MODIS measurements [31] to match data from both thermal infrared radiometers. To align Landsat-8 and MODIS pixels, we adopted a method that reduces Landsat-8 resolution. Initially, we determined the position of Landsat-8 orbits within MODIS images. For each Landsat-8 pixel, a MODIS pixel was selected based on the nearest Euclidean distance. Given Landsat-8's spatial resolution of 30 m and MODIS's resolution of 1000 m, numerous Landsat-8 points exist within a single MODIS pixel. Therefore, we computed the arithmetic mean of Landsat-8 pixels within the MODIS pixel, considering the average L_t from Landsat-8 pixels corresponding to the MODIS SST pixel.

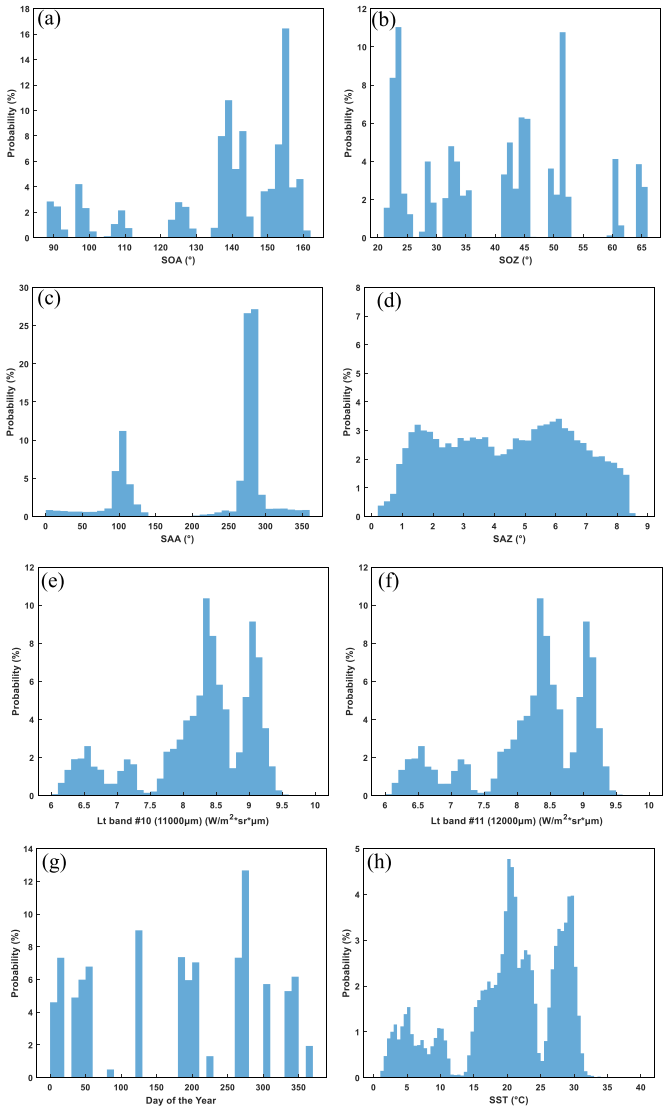

Fig. 3. (a)–(g) Frequency distribution histograms of the dataset designed by the model. (h) Range covered by the SST within the dataset.

For any machine learning scheme, inclusive and representative data used for training are the key to model performance. Fig. 3 shows the range of SST, L_t, SOA, SOZ, SAA, SAZ, and the day of year, indicating a strong inclusiveness and wide range of representativity of data used in this effort.

C. In Situ Data

Xiamen environmental monitoring station routinely records SST at four buoys from January 2021 to May 2023, with locations of these buoys shown in Fig. 4. These buoys, equipped with the EXO Sondes thermometers, can measure various parameters of the water column at 30-min intervals, including temperature, dissolved oxygen concentration, and pH value, transmitting the collected data to the main module for processing and storage. The temperature gauge has a detection range of -5 to 50 °C, with a temperature resolution of 0.001 °C. These specifications

[1] [Online]. Available: https://earthexplorer.usgs.gov.
[2] [Online]. Available: https://oceancolor.gsfc.nasa.gov/.

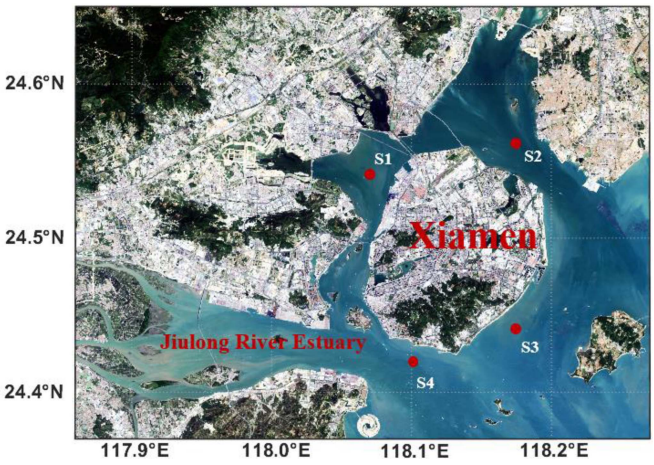

Fig. 4. Location of environmental monitoring buoys in Xiamen bay. Here we used the Mercator projection.

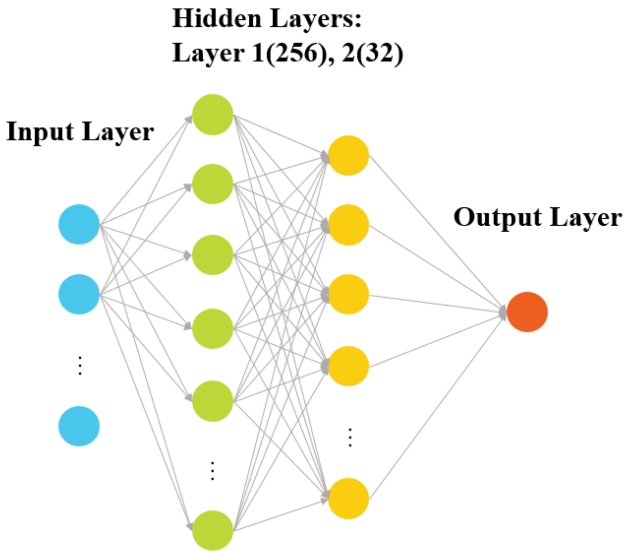

Fig. 5. Framework of NN_for_L8-SST.

TABLE I
INPUT AND OUTPUT OF NN_FOR_L8-SST

Input	Output
L_t from Band #10	
L_t from Band #11	
SOZ	
SOA	SST
SAZ	
SAA	
Day of the year	

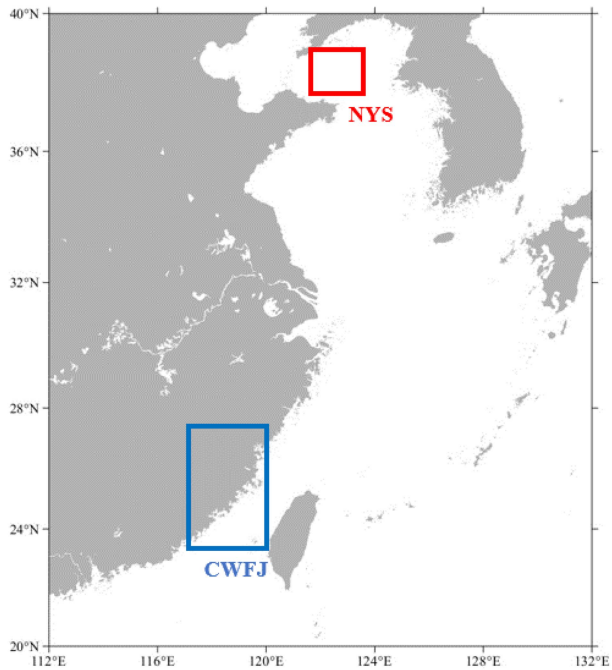

Fig. 6. Regions (the red and blue boxes) where both Landsat-8 and MODIS data were used for algorithm development.

ensure high sensitivity and measurement accuracy of the sensor. The four buoy stations utilized in this study are located at Baozhuyu Island (S1), Tong'an Bay (S2), Coconut Wind Zhai (S3), and Hulishan Fortress (S4), primarily situated around Xiamen Island, China, covering different geographical conditions and water characteristics of the bay, lending support to the data's representativeness.

III. METHODS

A. Structure of NN for Landsat-8 SST (NN_for_L8-SST)

For the development of a NN algorithm to retrieve SST from Landsat-8 measurements, the Multilayer Perceptron (MLP), a common structure within artificial neural networks used for machine learning, was employed. It comprises multiple layers of neurons, including an input layer, at least one or more hidden layers, and an output layer. MLP undergoes training via the back-propagation algorithm, adjusting weights continuously using known input–output pairs from training samples to minimize the error between predicted and actual values. This process involves gradient descent optimization, updating weights by computing gradients of the loss function, and progressively enhancing the model's accuracy.

NN_for_L8-SST has 7 inputs: L_t from Band #10, Band #11, SOZ, SOA, SAZ, SAA, and the day of the year (see Table I). The thermal infrared window bands around 11 and 12 μm are vital elements for the retrieval of SST [32]. Observational angles such as solar and satellite zenith and azimuth angles play a significant role in calibrating the consistency of L_t under various observational conditions, thus holding substantial importance for the accurate retrieval of SST [33]. The day of the year provides information on seasonality and other periodic changes related to SST [34]. This information is crucial for developing predictive models and algorithms. To find the optimal number of hidden layers and neurons, we experimented with various

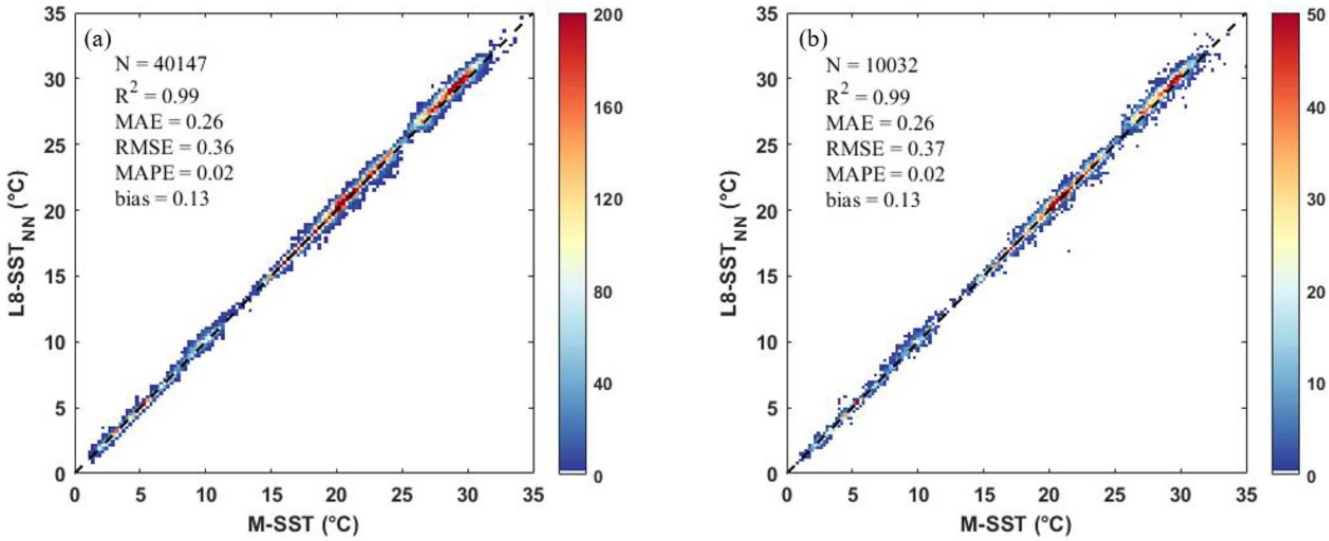

Fig. 7. (a) Comparison (density plot) between L8-SST_{NN} and M-SST for the training subset; (b) as (a), for the testing subset.

TABLE II
DATE INFORMATION OF THE TRAINING DATASET

CWFJ		NYS
2015/01/14	2021/02/15	2013/03/25
2016/07/27	2021/02/22	2013/07/03
2017/08/15	2021/07/09	2014/05/03
2018/10/05	2021/09/20	2015/01/30
2018/10/30	2021/11/04	2017/10/02
2019/12/11	2021/11/30	2018/01/06
2020/05/03		2019/12/27

TABLE III
DATE INFORMATION OF THE EVALUATION DATASET

CWFJ	NYS
2018/10/21	2013/04/14
2019/08/21	2013/05/16
2020/03/16	2013/08/20
2021/01/14	2014/09/08
2021/07/25	2023/02/05
2021/12/16	2023/04/26
2022/09/30	

combinations. Based on performance and computational efficiency, an optimal configuration to train NN_for_L8-SST was determined, which has 2 hidden layers, configured with 256 and 32 neurons, respectively (see Fig. 5). The output layer consisted of a single node for SST. In each hidden layer, we implemented the Leaky Rectified Linear Unit (LeakyReLU) as the activation function. LeakyReLU allows for a small positive slope with negative inputs, addressing the issue of vanishing gradients while retaining the network's nonlinear characteristics. Adam optimizer [35] was chosen to minimize the loss function. The adaptive nature of the Adam optimizer in adjusting learning rates and parameters contributes to enhancing the convergence speed and overall performance of the network. For training the network, a learning rate of $2{*}e^{-4}$ and a batch size of 8 were set, and the network was trained for 400 iterations. Adam can effectively reduce the impact of hyperparameter tuning on the model, with the loss function reaching relative stability at the end of training [36]. These parameters were fine-tuned through multiple experiments to ensure optimal model performance.

In this work, we did not include water vapor as one of the inputs, primarily due to that there is no water-vapor product matching the resolution of Landsat-8. The presently used low-resolution (0.625° × 0.5°) water-vapor product to produce L8-L2ST might be a major source of uncertainties. In addition, lower-resolution input will obscure other high-resolution data [37]. Further, inadequate data input could add complexity to the NNs, impact training effectiveness, and result in more uncertainties [38].

B. Data for Training and Testing NN_for_L8-SST

The training dataset for NN_for_L8-SST consists of 13 Landsat-8 images from coastal waters of Fujian Province, China (CWFJ) and 7 images from the northern part of the Yellow Sea (NYS) (see Fig. 6), where the information of these images are provided in Table II. SST in these regions ranges approximately 0–35 °C across the four seasons. This training dataset is divided into an 80% training subset and a 20% testing subset.

C. Accuracy Assessment

For statistical evaluation, the algorithm's performance is assessed by four metrics, which include the coefficient of determination (R^2) in linear regression analysis, mean absolute error

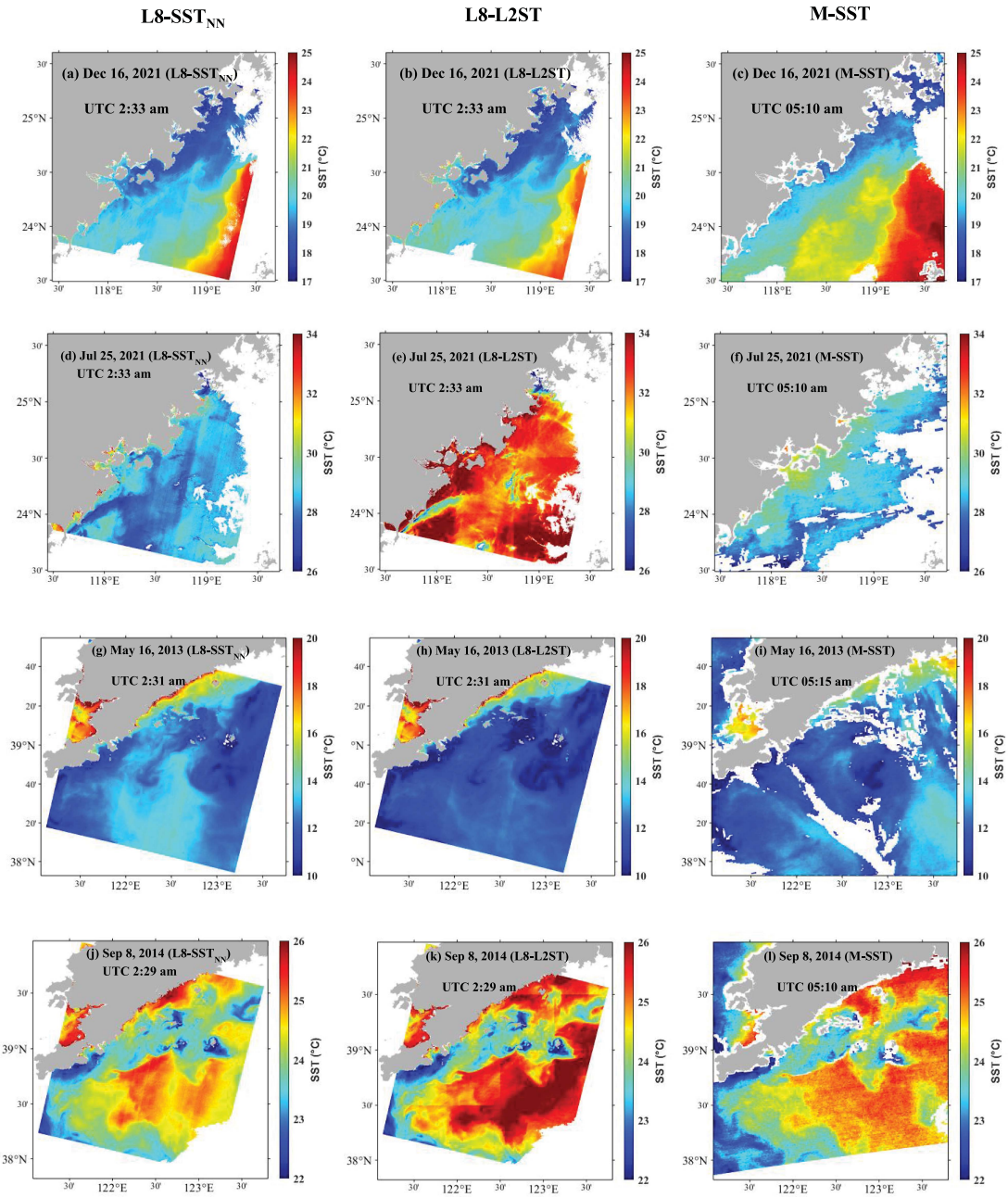

Fig. 8. Examples of L8-SST$_{NN}$ covering four seasons and its comparison with L8-L2ST and M-SST. The first column represents L8-SST$_{NN}$, the second column represents L8-L2ST, and the third column represents M-SST. Each row corresponds to images taken on the same day, which are 16 December 2021, 25 July 2021, 16 May 2013, and 8 Sep 2014.

(MAE), root mean square error (RMSE), mean absolute percentage error (MAPE), and mean difference (bias). MAE measures the average absolute deviation between estimated results and observed values, aiding in evaluating the predictive accuracy and stability of the model. RMSE is employed to evaluate the overall accuracy of the model's predictions and its fit to the data. MAPE provides a measure of the relative difference between predicted and observed values. These metrics are computed as follows:

$$\mathrm{RMSE} = \sqrt{\frac{1}{N}\sum_{1}^{N}(y-\tilde{y})^2} \tag{1}$$

$$\mathrm{MAE} = \frac{1}{N}\sum_{1}^{N}|y-\tilde{y}| \tag{2}$$

$$\mathrm{MAPE} = \frac{1}{N}\sum_{1}^{N}\left|\frac{y-\tilde{y}}{\tilde{y}}\right| * 100\% \tag{3}$$

$$\mathrm{bias} = \frac{1}{N}\sum_{1}^{N}(y-\tilde{y}) \tag{4}$$

where N denotes the number of data points, y represents the estimated SST value, and $\tilde{y}$ represents the reference or measured SST used for comparison.

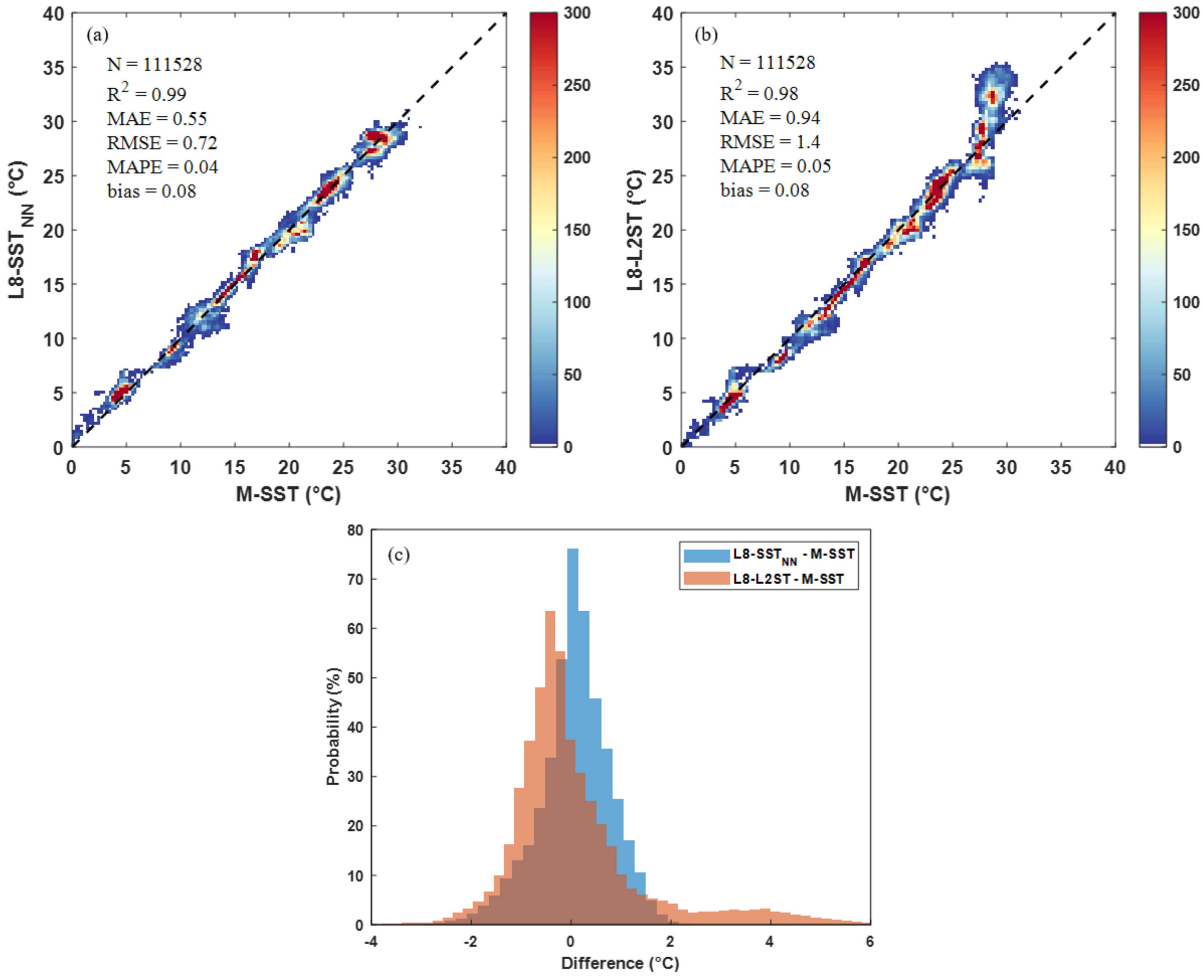

Fig. 9. Quantitative comparison of estimated SST for the evaluation dataset. (a) Density plot between L8-SST_{NN} and M-SST. (b) Density plot between L8-L2ST and M-SST. (c) Distributed frequency of histograms of the SST differences (L8-SST_{NN} – M-SST, and L8-L2ST – M-SST, respectively).

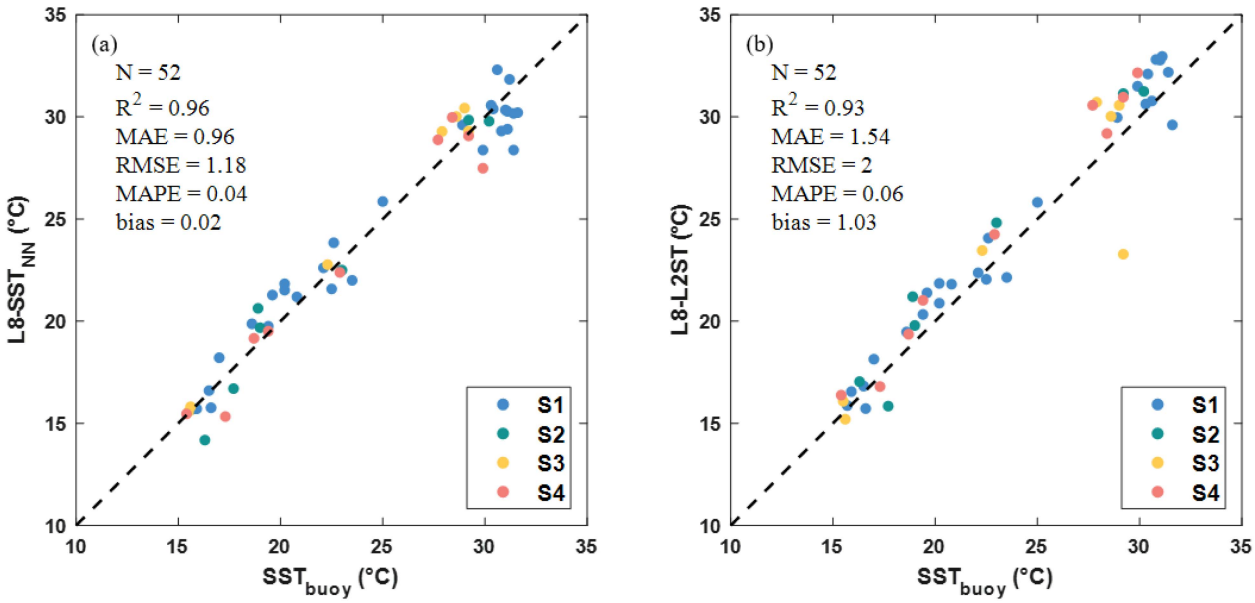

Fig. 10. Comparison of satellite-derived SST with SST_{buoy}. (a) Between L8-SST_{NN} and SST_{buoy}. (b) Between L8-L2ST and SST_{buoy}.

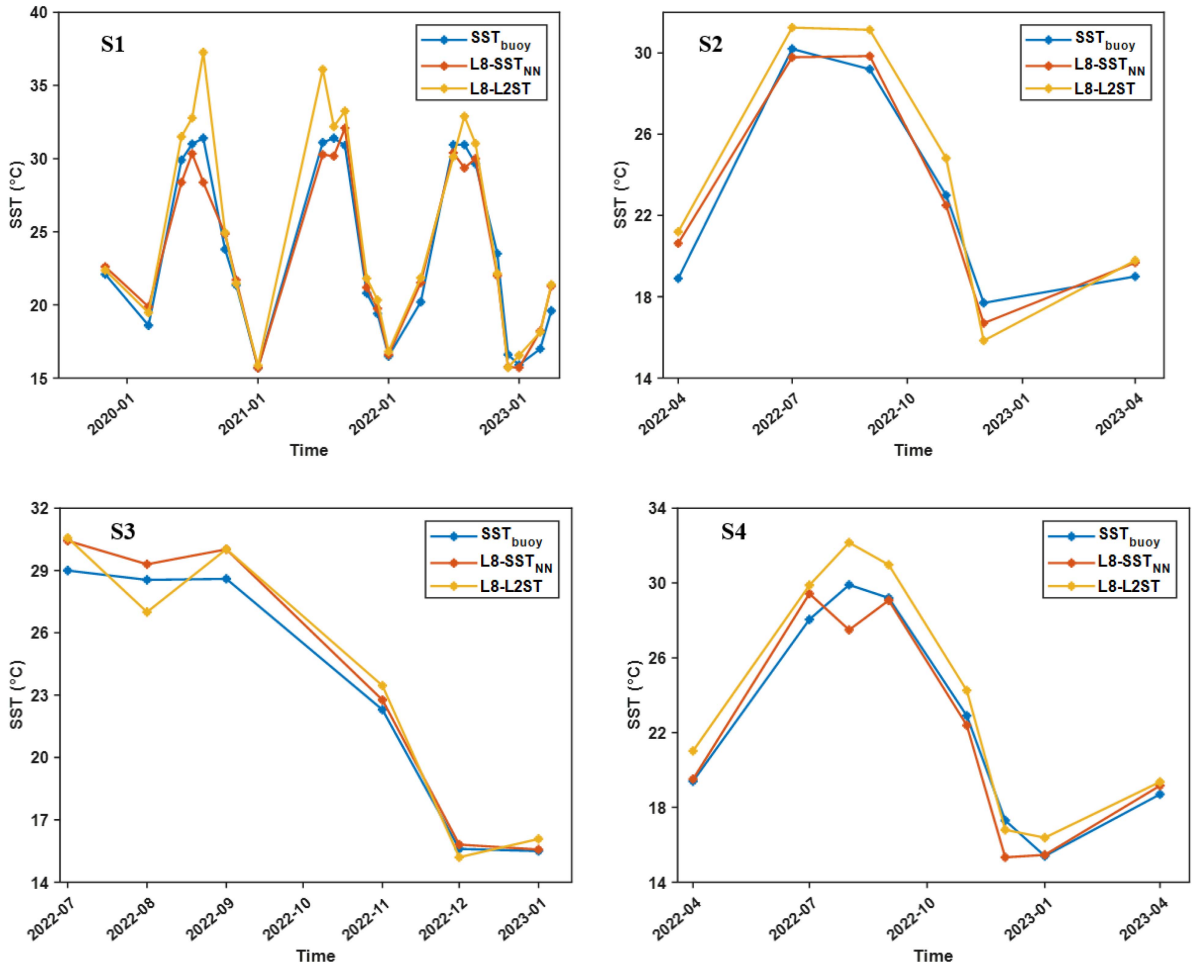

Fig. 11. Temporal variations of SST_{buoy}, L8-SST_{NN}, and L8-L2ST of the four stations.

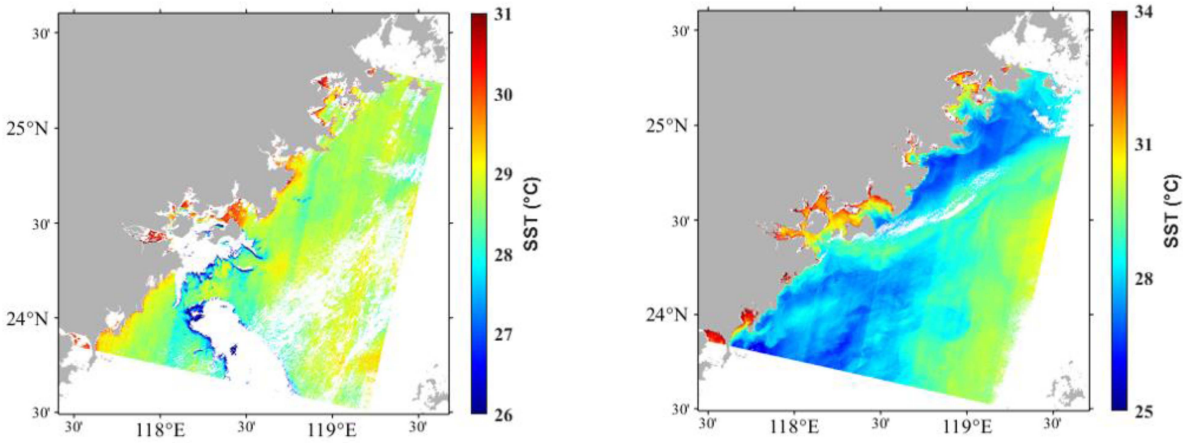

Fig. 12. Corresponding L8-SST_{NN} images for the two scenes in Fig. 1.

IV. Results

A. Results of the Training and Testing Datasets

Numerous studies have demonstrated excellent capabilities of NNs, so do here, where Fig. 7(a) compares SST from Landsat-8 obtained by the NNs (represented as L8-SST_{NN}) with MODIS-SST (represented M-SST in the following) for the training subset, with Fig. 7(b) for the testing subset. For M-SST in a range of ∼2–34 °C, the R^2 values are greater than 0.99, with RMSE as 0.36 and 0.37 °C, respectively, for the training and testing datasets. These outcomes highlight the strong capability of NN_for_L8-SST in estimating SST from Landat-8 measurements.

B. Extensive Comparison With L8-L2ST and M-SST

To get a more complete picture of the performance of NN_for_L8-SST, this NN algorithm was further applied to 13 Landsat-8 images (covering four seasons) collected over the coastal region of CWFJ and NYS, China, where these images were not involved in the training of NN_for_L8-SST. We named these images as the evaluation dataset. The date information of these images is provided in Table III. Fig. 8 shows four images of the resulting L8-SST_{NN} images, along with L8-L2ST and M-SST for comparison. Generally, as presented by the three SST products, it appears that SST is higher offshore in winter and spring, but nearshore waters are warmer during summer and fall.

Taking M-SST as a reference (in a range of ∼2–34 °C), we observed excellent consistency between L8-SST_{NN} and M-SST [see Fig. 9(a)]. Statistically, the R^2 value is 0.99, with RMSE as 0.72 °C, which highlights that the two sensors produced SST with higher accuracy compared to conventional products, at least for these regions. For the same Landsat-8 and MODIS data, however, the R^2 value becomes 0.98, with RMSE as 1.4 °C between L8-L2ST and M-SST [see Fig. 9(b)]. In particular, L8-L2ST appeared ∼3 °C higher than M-SST when the latter is around 30 °C. Further, Fig. 9(c) presents the histogram of SST differences (L8-SST_{NN} – M-SST, in blue color; L8-L2ST – M-SST, in orange color). It is found that the difference between L8-SST_{NN} and M-SST is centered around 0 °C, but the difference between L8-L2ST and M-SST shows two modes, one around -0.7 °C, another at ∼3.5 °C. The two modes are the results of lower L8-L2ST for M-SST in a range of ∼5–20 °C, but higher L8-L2ST for M-SST over ∼27 °C [see Fig. 9(b)]. In particular, L8-L2ST shows wider deviations when SST is around 30 °C. These results highlight that better consistency is achieved between L8-SST_{NN} and M-SST, than that between L8-L2ST and M-SST. This contrast, in part, is because L8-SST_{NN} was trained using M-SST, while L8-L2ST was obtained independent of M-SST, in addition to the different measurements and algorithms used.

However, L8-SST_{NN} exhibits stronger stripping effects, possibly due to the utilization of data from the thermal infrared Band #11, unlike the single-band method employed for L8-L2ST products (which used Band #10). The use of a single band helps mitigate the stripping effect, while utilizing two bands is advantageous for capturing details in the thermal infrared bands and atmospheric information.

C. Validation Using In Situ Data

Further, we evaluated L8-SST_{NN} with SST from buoy measurements (SST_{buoy}), along with a comparison between L8-L2ST and SST_{buoy}. These buoy data were obtained from the four stations shown in Fig. 4, from January 2021 to May 2023. These four buoy sites are of distinct geographical locations and water quality characteristics. Both S1 and S2 are located on the northern side of Xiamen Island, situated between the island and the mainland. In contrast, S3 and S4 are located on the southern side of Xiamen Island, which is open to the Taiwan Strait. In addition, S4 is subject to the influence of the Jiulong River. All these pose strong challenges to traditional schemes in estimating SST from satellite measurements, especially when its resolution is low. The measurement depth of SST_{buoy} is about 20 cm below sea surface, which may not exactly reflect "surface temperature" [39], but should be representative enough for this dynamic region.

For SST_{buoy} in a range of 15–34 °C, L8-SST_{NN} showed excellent agreement [see Fig. 10(a)]. In linear statistical analysis, the R^2 value is 0.96 (N = 52), with MAE under 1 °C, and MAPE under 5%. These results, along with the results when comparing with M-SST, indicate excellent performance of NN_for_L8-SST. In the meantime, for the same *in situ* measurements, a comparison between L8-L2ST and SST_{buoy} also shows very good agreement [see Fig. 10(b)], but the statistical measures are slightly worse than that between L8-SST_{NN} and SST_{buoy}.

In another way to show consistency among the SST data, Fig. 11 shows temporal variations of SST of the four stations obtained *in situ*, along with the temporal variation of L8-SST_{NN} and L8-L2ST. For Station S1, which has measurements of ∼4 years, L8-SST_{NN} captured the temporal pattern of *in situ* SST excellently, but L8-L2ST overestimated SST for two summer periods (2021 and 2022). The time span of the other three stations is much shorter (∼1 year), where L8-SST_{NN} and L8-L2ST also show excellent agreement with SST_{buoy} in temporal variations. The excellent agreement between SST_{buoy} and L8-SST_{NN} for the four stations further demonstrates that although NN_for_L8-SST used M-SST as the data source for training, the resulting SST is not biased, rather in great agreement with field-measured SST, even for complex waters surrounding Xiamen Island, China.

D. "Checkerboard" Images

For the two L8-L2ST images shown in Fig. 1 that have "checkerboard" patterns, their L8-SST_{NN} products are shown in Fig. 12, where no such "checkerboard" patterns appeared. This shows that as NN for L8-SST bypassed the traditional approach for SST estimation that requires much information related to the atmosphere, where no high-resolution for such data is available, therefore no extra sources of uncertainties are introduced, subsequently no "checkerboard" pixels in the resulting SST images. This result, along with the above evaluations, indicates that the NN scheme developed in this study is very effective in obtaining SST from Landsat-8 measurements, especially for regions with missing or less accurate atmospheric auxiliary data.

V. Summary

In this research, utilizing MODIS SST data product as the reference, we developed a NN-based algorithm (NN_for_L8-SST) to estimate SST from Landsat-8 top-of-atmosphere radiance measurements. This scheme bypassed the complex data processing in estimating SST via the traditional radiative-transfer-based approach and avoided issues arising from mismatches in spatial resolution between Landsat-8 measurements and auxiliary data required for traditional data processing. The mismatch in spatial resolution degrades SST data product as shown in the standard

L8-L2ST product. For SST in a range of ∼2–34 °C, it is found that SST from NN_for_L8-SST matched very well with that from MODIS SST. Further, SST from NN_for_L8-SST showed excellent agreement with that from buoy measurements taken in waters around Xiamen Island, China. These results indicate that, although NN_for_L8-SST used MODIS SST as the reference for training, the resulting SST product is not biased, at least for the CWFJ and NYS. As MODIS is in its final years of service, we envision that this scheme could be extended to SST from other available mature satellites (e.g., VIIRS), thus obtaining highly accurate, high-spatial resolution, SST products from sensors like Landsat-8.

ACKNOWLEDGMENT

The authors would like to thank NASA for providing the Level-2 MODIS products, USGS for providing Level-1 Landsat-8 products, and Xiamen Environmental Monitoring Station for buoy data. We also thank three anonymous reviewers for their constructive comments and suggestions. All satellite data used in this study are available from NASA (https://oceancolor.gsfc.nasa.gov/) or EarthExplorer platform (https://earthexplorer.usgs.gov).

REFERENCES

[1] C. Vancutsem et al., "Evaluation of MODIS land surface temperature data to estimate air temperature in different ecosystems over Africa," *Remote Sens. Environ.*, vol. 114, no. 2, pp. 449–465, 2010.

[2] V. Banzon et al., "A long-term record of blended satellite and in situ sea-surface temperature for climate monitoring, modeling and environmental studies," *Earth Syst. Sci. Data*, vol. 8, no. 1, pp. 165–176, 2016.

[3] V. C. Slonosky, P. D. Jones, and T. D. Davies, "Atmospheric circulation and surface temperature in Europe from the 18th century to 1995," *Int. J. Climatol.*, vol. 21, no. 1, pp. 63–75, 2001.

[4] K. Cowtan et al., "Robust comparison of climate models with observations using blended land air and ocean sea surface temperatures," *Geophysical Res. Lett.*, vol. 42, no. 15, pp. 6526–6534, 2015.

[5] M. L. L'Heureux, D. C. Collins, and Z.-Z. Hu, "Linear trends in sea surface temperature of the tropical Pacific Ocean and implications for the El Niño-Southern Oscillation," *Climate Dyn.*, vol. 40, no. 5–6, pp. 1223–1236, 2012.

[6] P. C. Reid and G. Beaugrand, "Global synchrony of an accelerating rise in sea surface temperature," *J. Mar. Biol. Assoc. United Kingdom*, vol. 92, no. 7, pp. 1435–1450, 2012.

[7] T. R. Loveland and J. R. Irons, "Landsat 8: The plans, the reality, and the legacy," *Remote Sens. Environ.*, vol. 185, pp. 1–6, 2016.

[8] D. P. Roy et al., "Landsat-8: Science and product vision for terrestrial global change research," *Remote Sens. Environ.*, vol. 145, pp. 154–172, 2014.

[9] J. Tavora et al., "Recipes for the derivation of water quality parameters using the high-spatial-resolution data from sensors on board sentinel-2A, sentinel-2B, Landsat-5, Landsat-7, Landsat-8, and Landsat-9 satellites," *J. Remote Sens.*, vol. 3, 2023, Art. no. 49.

[10] P. J. Minnett et al., "Half a century of satellite remote sensing of sea-surface temperature," *Remote Sens. Environ.*, vol. 233, 2019, Art. no. 69.

[11] J. C. Jimenez-Munoz, J. Cristobal, J. A. Sobrino, G. Soria, M. Ninyerola, and X. Pons, "Revision of the single-channel algorithm for land surface temperature retrieval from Landsat thermal-infrared data," *IEEE Trans. Geosci. Remote Sens.*, vol. 47, no. 1, pp. 339–349, Jan. 2009.

[12] M. Liu, C. J. Merchant, O. Embury, J. Liu, Q. Song, and L. Guan, "Retrieval of sea surface temperature from HY-1B COCTS," *IEEE Trans. Geosci. Remote Sens.*, vol. 60, 2022, Art. no. 5002913.

[13] C. C. Walton et al., "The development and operational application of nonlinear algorithms for the measurement of sea surface temperatures with the NOAA polar-orbiting environmental satellites," *J. Geophysical Res., Oceans*, vol. 103, no. C12, pp. 27999–28012, 1998.

[14] C. J. Merchant et al., "Optimal estimation of sea surface temperature from split-window observations," *Remote Sens. Environ.*, vol. 112, no. 5, pp. 2469–2484, 2008.

[15] Q. Vanhellemont, "Automated water surface temperature retrieval from Landsat 8/TIRS," *Remote Sens. Environ.*, vol. 237, pp. 49–62, 2020.

[16] E. Alerskans et al., "Construction of a climate data record of sea surface temperature from passive microwave measurements," *Remote Sens. Environ.*, vol. 236, 2020, Art. no. 111485.

[17] X. Yu et al., "A novel method for sea surface temperature prediction based on deep learning," *Math. Problems Eng.*, vol. 2020, pp. 1–9, 2020.

[18] S. Kartal, "Assessment of the spatiotemporal prediction capabilities of machine learning algorithms on sea surface temperature data: A comprehensive study," *Eng. Appl. Artif. Intell.*, vol. 118, 2023, Art. no. 026520.

[19] S. Xu and J. Cheng, "A new land surface temperature fusion strategy based on cumulative distribution function matching and multiresolution Kalman filtering," *Remote Sens. Environ.*, vol. 254, 2021, Art. no. 112256.

[20] M. A. Syariz et al., "Retrieval of sea surface temperature over poteran island water of Indonesia with Landsat 8 tirs image: A preliminary algorithm," *Int. Arch. Photogram., Remote Sens. Spatial Inf. Sci.*, vol. XL-2/W4, pp. 87–90, 2015.

[21] C. Du et al., "A practical split-window algorithm for estimating land surface temperature from Landsat 8 data," *Remote Sens.*, vol. 7, no. 1, pp. 647–665, 2015.

[22] S. Guha et al., "Analytical study of land surface temperature with NDVI and NDBI using Landsat 8 OLI and TIRS data in Florence and Naples city, Italy," *Eur. J. Remote Sens.*, vol. 51, no. 1, pp. 667–678, 2018.

[23] L. Wei, L. Guan, and L. Qu, "Prediction of sea surface temperature in the South China Sea by artificial neural networks," *IEEE Geosci. Remote Sens. Lett.*, vol. 17, no. 4, pp. 558–562, Apr. 2020.

[24] M. Montanaro et al., "Stray light artifacts in imagery from the Landsat 8 thermal infrared sensor," *Remote Sens.*, vol. 6, no. 11, pp. 10435–10456, 2014.

[25] J. F. Mas and J. J. Flores, "The application of artificial neural networks to the analysis of remotely sensed data," *Int. J. Remote Sens.*, vol. 29, no. 3, pp. 617–663, 2007.

[26] X. Li, Y. Zhou, and F. Wang, "Advanced information mining from ocean remote sensing imagery with deep learning," *J. Remote Sens.*, vol. 2022, 2022, Art. no. 9849645.

[27] Q. Liu et al., "Deep contrastive learning network for small-sample hyperspectral image classification," *J. Remote Sens.*, vol. 3, 2023, Art. no. 263580.

[28] S. Wolff, F. O'Donncha, and B. Chen, "Statistical and machine learning ensemble modelling to forecast sea surface temperature," *J. Mar. Syst.*, vol. 208, 2020, Art. no. 103347.

[29] Q. Vanhellemont et al., "Validation of Landsat 8 high resolution sea surface temperature using surfers," *Estuarine, Coastal Shelf Sci.*, vol. 265, 2022, Art. no. 107650.

[30] W. Lai et al., "A portable algorithm to retrieve bottom depth of optically shallow waters from top-of-atmosphere measurements," *J. Remote Sens.*, vol. 2022, 2022, Art. no. 2567650.

[31] P. J. Minnett, "Consequences of sea surface temperature variability on the validation and applications of satellite measurements," *J. Geophysical Res., Oceans*, vol. 96, no. C10, pp. 18475–18489, 2012.

[32] O. B. Brown et al., "MODIS infrared sea surface temperature algorithm algorithm theoretical basis document version 2.0," *Univ. Miami*, vol. 31, pp. 098–033, 1999.

[33] R. Niclòs et al., "Determination of sea surface temperature at large observation angles using an angular and emissivity-dependent split-window equation," *Remote Sens. Environ.*, vol. 111, no. 1, pp. 107–121, 2007.

[34] S. Sunder, R. Ramsankaran, and B. Ramakrishnan, "Machine learning techniques for regional scale estimation of high-resolution cloud-free daily sea surface temperatures from MODIS data," *ISPRS J. Photogram. Remote Sens.*, vol. 166, pp. 228–240, 2020.

[35] Z. Zhang, "Improved Adam optimizer for deep neural networks," in *IEEE/ACM 26th Int. Symp. Qual. Service*, 2018, pp. 1–2.

[36] P. T. Sivaprasad et al., "Optimizer benchmarking needs to account for hyperparameter tuning," in *Proc. 37th Int. Conf. Mach. Learn.*, 2020, pp. 9036–9045.

[37] G. Singh and E. Kumar, "Input data scale impacts on modeling output results: A review," *J. Spatial Hydrol.*, vol. 13, no. 1, 2017, Art. no. 106504.

[38] G. Paris, D. Robilliard, and C. Fonlupt, "Exploring overfitting in genetic programming," in *Artificial Evolution*. Berlin, Germany: Springer, 2004.

[39] H. Zhang et al., "Seasonal patterns of SST diurnal variation over the Tropical warm pool region," *J. Geophysical Res., Oceans*, vol. 121, no. 11, pp. 8077–8094, 2016.